The influence of a sub-lithospheric layer width on the partitioning of the induced mantle flow, surface motions and subduction dynamics

R. Carluccio[a], L. N. Moresi[b], F. A. Capitanio [c], R. Farrington[a], L. Colli[d], B. R. Mather[8]

[a]School of Geography, Earth and Atmospheric Sciences, University of Melbourne, VIC, AU
[b]Research School of Earth Sciences, Australian National University, Canberra, ACT, AU
[c]School of Earth, Atmosphere and Environment, Monash University, Clayton, VIC, AU. Melbourne, VIC, AU
[d] Department of Earth and Atmospheric Sciences, University of Houston, Houston, TX, US
[e]EarthByte Group, School of Geoscience, The University of Sydney, Sydney, NSW, AU.

Highlights

- Geophysical observations suggest the presence of a very thin and weak sub-lithospheric layer (SLL) beneath some segments of the subducting Pacific lithosphere, but little is known about its lateral extent.
- Numerical models show that variation in SLL width can alone introduce significant toroidal flow, which has proven difficult to achieve in previous subduction numerical studies without a free-edge slab.
- Regional variations in SLL width and viscosity provide an alternative and novel mechanism for the generation of toroidal motion from buoyant convection.

Abstract

The partitioning of the three-dimensional mantle flow into toroidal and poloidal components is a diagnostic element to characterise tectonics regimes, with both fields being substantially active and representative of the contemporary mode of mantle convection. The toroidal:poloidal ratio (T/P) affects several aspects of mantle circulation, including the sinking of the subducting lithosphere into the mantle and the lateral transport of melt and volatiles around the subduction zone. Geophysical observations suggest the presence of a very weak and thin sub-lithospheric layer (SLL) underneath several segments of the subducting Pacific lithosphere; however very little is known about its lateral extent. To address the impact of an SLL on mantle circulation in three dimensions, we perform buoyancy-driven subduction numerical models where we introduce an SLL and systematically vary its width and viscosity. Our results show that a non-uniform SLL produces a variety of subduction regimes and significant T/P (0.18-0.52). Most importantly, a considerable toroidal flow component is found in models where the slab has no free edge, where the deformation field would otherwise be completely poloidal, and the toroidal component is suppressed. As such, these outcomes provide a novel contribution to the long-standing debate on the link between the slab pull driving force in buoyant convection and the generation of toroidal flow. Furthermore, these findings aid the interpretation of subduction zones characterised by lateral variability in slab (c-to-s) morphology and trench (advance-to-retreat) migration where geophysical studies have reported an SLL, including Mariana, Izu-Bonin, and Nazca subduction regions, among others.

1 Introduction

The lithosphere, the solid Earth's uppermost layer, is fragmented into a series of strong major and minor tectonic plates moving over a weaker and more buoyant layer of asthenospheric material. At subduction zones, the negative buoyancy of slabs, resisted by the drag of the surrounding viscous mantle, drives the motion and deformation of the tectonic plates and the global mantle circulation (e.g., Forsyth et al., 1975; Lithgow-Bertelloni and Richards, 1995; Conrad and Lithgow-Bertelloni, 2002). The resistance to shearing acting at the lithosphere-asthenosphere boundary (LAB) plays a critical role in influencing the force balance around the subducting plate and the degree of mantle-lithosphere coupling processes (e.g., Forsyth et al., 1975; Anderson, 1995; Ribe, 1989; O'Connell et al., 1991; Lithgow-Bertelloni et al., 1993; Bokelmann, 2002; Natarov and Conrad, 2012). Recent geophysical studies have brought considerable attention to the structure of the asthenosphere at convergent margins (e.g., Kawakatsu et al., 2009; Naif et al., 2013; Hawley et al., 2016). These studies report the presence of an abrupt regional seismic velocity decrease and high electrical conductivity increase within a thin and weak sub-lithospheric layer (SLL) underneath several segments of the subducting oceanic lithosphere. Beneath the base of the subducting plate, melt-induced viscosity reductions can occur within one or multiple layers up to 50 km thick and lead up to a $\sim$4 orders of magnitude viscosity jump between the lithosphere and the underlying asthenosphere (e.g., Kawakatsu et al., 2009; Naif et al., 2013; Hawley et al., 2016). Two-dimensional numerical models have shown that an SLL can impact the partitioning of surface motions, subduction dynamics, and slab morphology in the lower mantle by significantly reducing the mechanical coupling between plate motions and mantle tractions (Carluccio et al., 2019; Cerpa et al., 2022).

While the enhanced melt content and/or presence of hydrated phases could significantly lubricate the base of the subducting lithosphere impacting surface motions and subduction dynamics, the complicated physical nature of the LAB and the trade-off that exists between power and lateral coverage of seismic methods hinder the ability to image the lateral extent of these channels. In this study, we focus on addressing the geodynamic role of the lateral extent of the SLL on the partitioning of the induced mantle flow, surface motions, and the subduction style using three-dimensional (3D) numerical models of subduction.

Any 3D velocity field associated with plate motions can be divided into poloidal and toroidal components for analysis (Forsyth et al., 1975; Lithgow-Bertelloni et al., 1993; Bercovici and Wessel, 1994; Tackley, 2000). Poloidal flow corresponds to convergence or divergence in a horizontal plane (e.g., back-arc and sea-floor spreading). It is associated with vertical mass transport and promotes the deformation of the overriding plate (Uyeda and Kanamori, 1979; Funiciello et al., 2003; Schellart and Moresi, 2013). Toroidal flow corresponds to a rotation in the horizontal plane around a vertical axis, and as such, it is associated with vertical vorticity (e.g., transform boundaries or plate rotation) (Tackley, 2000). The partitioning of the induced mantle flow is henceforth denoted as the amplitude ratio between the toroidal and poloidal components of the Earth's flow field, T/P. The 3D flow field partitioning is critically important for better understanding mantle circulation around the trench zone (e.g., Faccenda and Capitanio, 2012; Long, 2013) and particularly relevant for back-arc basin formation, melt- and volatiles-transport in the backarc, as well as overriding plate and subducting slab deformations (Forsyth et al., 1975; Uyeda and Kanamori, 1979; Long, 2013). The present-day average T/P depends on the choice of reference frame adopted and changes during geologic time (Čadek and Ricard, 1992; Lithgow-Bertelloni et al., 1993; Tackley, 2000). Nonetheless, no plate boundary is purely poloidal or toroidal but usually displays some combination of the two. Both flow fields are currently observed on Earth and strongly localised along plate boundaries with comparable peak values (O'Connell et al., 1991; Bercovici, 2003). Hence, the Earth's surface toroidal component is a relevant fraction of the whole flow field (Hager and O'connell, 1978; O'Connell et al., 1991; Lithgow-Bertelloni et al., 1993), although smaller than the poloidal component, having ranged between approximately 0.25 and 0.5 (excluding net rotation) in the last 120 million years (Olson and Bercovici, 1991; Lithgow-Bertelloni et al., 1993).

Buoyancy-driven fluids with only vertically layered viscosity do not generate any toroidal motion and lateral variable viscosity convection (e.g., with constant, depth-dependent or temperature-dependent viscosity) calculations typically produce only a limited amount of T/P (Christensen and Harder, 1991; Tackley, 2000). There is apparently no direct link between the driving slab pull force in buoyant convection (which drives only vertical and divergent motion) and the development of toroidal flow. The challenge of how to trigger buoyancy-driven flow to induce and self-sustain the generation of toroidal flow, either through horizontal viscosity variations or boundary conditions (i.e., imposing plates, faults, or strain weakening effects at plate margins) represents the so-called “poloidal–toroidal coupling problem” and remains an open issue in understanding the generation of Earth's plate-tectonic style of mantle convection (Bercovici et al., 2015).

It has been proposed that the degree of lithosphere-mantle coupling processes could contribute to the amount of toroidal flow observed at plate boundaries (e.g., Bercovici and Wessel, 1994; O'Connell et al., 1991; Gable et al., 1991). Global convection models show that the inclusion of a thickened low viscosity zone (LVZ) - the asthenosphere - favours plate-like behaviour; however, they also reveal smaller effects on the global net rotation and observed patterns of global seismic anisotropy (Tackley, 2000; McNamara et al., 2010). On the other hand, a thin SLL could accommodate horizontal shearing and gravitational sliding of the lithosphere much better than distributed vertical loading or unloading over regions significantly larger than the layer's depth (Scoppola et al., 2006; Carluccio et al., 2019). Hence, variations in SSL viscosity and their spatial distributions could influence how the deformation flow induced in the mantle by the sinking slab is split between its vertical and lateral flow, playing a fundamental role in subduction geodynamics.

Previous 3D modelling work has shown how the subduction of an oceanic plate into the underlying mantle is accommodated by both the poloidal and the toroidal flow components (e.g., Conrad and Hager, 1999; Kneller and Van Keken, 2008; Piromallo et al., 2006). The relative contribution of each component depends upon lateral variations in plate and trench widths (Funiciello et al., 2004; Schellart et al., 2007; Stegman et al., 2006), temperature distribution around the slab, plate age and strength (Kincaid and Griffiths, 2003, 2004; Goes et al., 2011), slab and mantle viscosity and buoyancy contrast (Capitanio et al., 2007; Conrad and Hager, 1999; Kneller and Van Keken, 2008; Piromallo et al., 2006), lithosphere-mantle rheology (Pusok et al., 2018; Billen and Hirth, 2005), initial conditions in a spherical spontaneously driven subduction (Crameri and Tackley, 2014), the inclusion of an oceanic plateau (Moresi et al., 2014; Pusok and Kaus, 2015), multiple slabs interacting with each other (Király et al., 2017) and with the overriding plate (Sternai et al., 2014), double subduction systems (Pusok and Stegman, 2019), as well as plate geometry (Bercovici and Wessel, 1994; Kneller and Van Keken, 2008). These factors have been shown to influence mantle displacement around the subducting slab and contribute to the curvature, migration, and dynamics of a subduction zone (e.g., Funiciello et al., 2008; Faccenna et al., 2010; Long, 2013). While each component of a subduction system is fundamental and contributes to the evolution of mantle flow and slab deformation, a clear understanding of the relative control of SLL width on the partitioning of mantle circulation and its relationship with subduction surface motion, and subduction dynamics has yet to be resolved. In this study, we vary the viscosity and width of the SLL to determine the relative controls on slab and trench curvature and shape, trench and plate migration rates, and partitioning and evolution of mantle flow.

2 Method

To investigate the role of an SLL on subduction dynamics, we use the numerical code Underworld2, described in detail by Moresi et al. (2007) and Mansour et al. (2020). We adopt a pseudo-plastic rheology approximation and build upon the work of Carluccio et al. (2019) by expanding to the third dimension.

This approach uses Newtonian rheology everywhere but the oceanic crust of the subducting plate, which is visco-plastic. The visco-plastic layer acts as a lubricating phase to simulate the free surface and to allow the hinge of the bending plate to detach from the surface (e.g., Schmeling et al., 2008). When a

Newtonian constitutive relationship is implemented (for an incompressible fluid) the relationship between the deviatoric stress, τ_{ij}, and strain rate, η^{vs}, tensors is defined as:

$$\tau_{ij} = 2\eta^{vs}\dot{\varepsilon}_{ij} \tag{1}$$

where $\dot{\varepsilon}_{ij} = \frac{1}{2}\left(\frac{\partial v_i}{\partial x_j} + \frac{\partial v_j}{\partial x_i}\right)$ is the strain rate tensor. When plastic failure is considered for the uppermost layer, the total effective viscosity, η_{eff}, is taken as the minimum between the viscous, η^{vs}, and the plastic, η^{pl}, terms, as follows:

$$\eta_{\text{eff}} = min[\eta^{\text{vs}}, \eta^{\text{pl}}] \tag{2}$$

We implement Byerlee's law by assuming the so-called depth-dependent approximation of the Drucker-Prager yield criterion (Moresi and Solomatov, 1998; Tackley, 2000). In this case, the yield stress, τ_y, and the effective viscosity of the plastic branch, η_{pl}, are implemented as follow:

$$\tau_y = \tau_0 + \mu \text{P}_{\text{lith}} \tag{3a}$$

$$\eta_{\text{pl}} = \frac{\tau_y}{2\dot{\varepsilon}_{II}} \tag{3b}$$

where $\dot{\varepsilon}_{II} = \left(\frac{1}{2}\dot{\varepsilon}_{ij}\dot{\varepsilon}_{ij}\right)^{(1/2)}$ is the second invariant of the strain rate, τ_0 the cohesive strength, μ the friction coefficient, and $\text{P}_{\text{lith}} = \rho g z$ is the reference lithostatic pressure at depth, z, whereby ρ is the density of the oceanic lithosphere and g is gravity. We use a cohesion of 20 MPa, a friction angle of 30°, and a density contrast between the oceanic lithosphere and the underlying mantle of 80 kg/m^3, consistent with the values calculated in the study of Cloos (1993). We reproduce the evolution of a mature 70 Myr-old oceanic lithosphere and use the thermal age of the oceanic plate to compute its initial thickness. We neglect temperature diffusion as the duration of the experiment is approximately 14 million years and are modelling an established subduction zone.

Subduction dynamics and mantle flow are modelled in a Cartesian box that extends 4,000 km and 3,000 km in the horizontal X and Y directions, respectively, and 660 km in depth (Z). Our models are made of 4 layers. There is an oceanic crust (OC), an oceanic plate (OP), an SLL, and an underlying upper mantle (UM), as shown in figure 1a. The modelled SLL is located at the base of the oceanic plate and has a default thickness of 30 km.

The initial condition for the subducting plate includes an initial trench position 1,000 km away from the wall and a slab tip already penetrating the mantle, 257 km deep with a dip angle of 34° to the horizontal. We use a model domain of 256*64*64 elements with uniform grid spacing in each coordinate direction and verified the model outputs using a higher-resolution grid of 256*128*128. The velocity boundary conditions are free-slip everywhere to minimise the influence of the box sidewalls. We do not apply any kinematic boundary condition and subduction is thus dynamically initiated. The assigned values result in subduction velocities of 2-10 cm/yr (figures 2a, 3), and divergence and vorticity of ±200 Gyr (figures 6,7,9) are both in line with the average values predicted on Earth (e.g., Bercovici, 2003). The rheological and geometrical model setups are both described in detail in Carluccio et al. (2019). More information about initial and varied parameters in this study can be found in figure 1 and supporting table T1, respectively.

2.1 Induced flow characteristics

We decompose the 3D velocity field ($\mathbf{u}$) into its poloidal and toroidal components for analysis of the induced flow characteristics. Following previous work (e.g., Tackley, 2000; Piromallo et al., 2006; Stegman et al., 2006), the decomposition is carried out in two-dimensional slices by evaluating horizontal divergence and vertical vorticity in each 2D grid point in time and space during the subduction evolution of the experiment.

The horizontal divergence is calculated as:

$$\nabla_h = \left(\frac{\partial}{\partial x}, \frac{\partial}{\partial y} \right) \cdot \mathbf{u} \tag{4}$$

and the vertical component of vorticity as:

$$w_z = \hat{z} \cdot \nabla \times \mathbf{u} \tag{5}$$

The surface integral of the horizontal divergence and vorticity yields to their 2D scalars, which are the poloidal, Φ, and toroidal, Ψ, potentials.

We obtain the poloidal potential, Φ, by integrating ∇_h in an x-y plane at a depth of interest:

$$\Phi(t)|_{z=depth} = \oiint_{W(L)} \nabla_h(t)\,\mathrm{d}x\,\mathrm{d}y \tag{6}$$

and the toroidal potential, Ψ, is calculated by integrating w_z in an x-y plane at a depth of interest, as follows:

$$\Psi(t)|_{z=depth} = \oiint_{W(L)} w_z(t)\,\mathrm{d}x\,\mathrm{d}y \tag{7}$$

The toroidal:poloidal ratio is one of the most traditional quantities invoked to quantify plate-like behaviour and long-term mantle circulation (Tackley, 2000), and is simply:

$$T/P = \frac{\Psi}{\Phi} \tag{8}$$

We analyse mantle flow in the proximity of the surface, underneath the LAB, and in the vicinity of the 660 km discontinuity. The evaluation of the velocity field is carried out at least 3 elements away from a phase or a model boundary to avoid any potential numerical noise that could arise from abrupt changes in the physical properties of two adjacent layers.

To explore the relationships between the induced flow characteristics and subduction surface motions, we introduce the subduction partitioning parameter, V_T/V_P, as the ratio between trench migration and the horizontal plate velocities, V_T and V_P, respectively. When the partitioning of the induced mantle flow and surface motions are compared (e.g., figures 8 and 9), the evaluation is carried out during the initial temporal stage of the subduction evolution (0-7 Myr) to ensure that the interaction of the slab with the 660 km discontinuity does not influence the results (Carluccio et al., 2019).

We identify end-member cases that outline the mechanical effect of the SLL, by varying the ratio between SLL and oceanic plate width ($\mathrm{W}^*=\mathrm{W}_{SLL}/\mathrm{W}_{OP}$), between 0 and 1, and the viscosity ratio between SLL and upper mantle, $\eta_{\mathrm{SLL}}/\eta_{\mathrm{UM}}$, between 10^0 and 10^2. In our study, we use a simplified rheological and geometrical model setup that allows us to constrain the impact of an SLL alone. Furthermore, the chosen model setup with no free-edge slab, allows us to verify that models with no lateral viscosity variations, such as the reference model RM ($\mathrm{W}^* = 0$), as well as M4 and M8 ($\mathrm{W}^* = 1$), yield very small values of T/P, on the order of 10^{-2} (figures 4 and 7), indicating that when significant T/P variations are observed (10^0–10^{-1}) it is due to subduction dynamics and not a numerical artefact. We also performed a small number of additional numerical experiments to explore the extent to which some of our simplifications may influence our conclusions, such as the inclusion of the lower mantle (supporting figure 1) and the use of a model setup with a free-edge slab (figure 8). Also in these models, an SLL maintains a constant signature. The results obtained in our numerical simulations are systematically investigated through the analysis of the impact of SLL width and viscosity on: i) slab morphology and subduction partitioning; ii) comparison of the divergence and vorticity fields; iii) evolution through time of induced poloidal and toroidal potentials and flow field partitioning, and iv) applicability of our numerical outcomes to natural subduction zones.

3 Results

All our numerical experiments share three distinct stages of a subduction zone temporal evolution (figure 3), as observed in previous studies (e.g., Yamamoto et al., 2007; Stegman et al., 2006). During the first stage and until approximately 5 to 6 Myr, subduction is dynamically initiated and the slab accelerates while sinking into the mantle underneath. This stage is followed by a deceleration phase due to the slab tip interaction with the upper-lower mantle transition zone which lasts until ∼6–8 Myr. After this period, subduction reaches a steady state configuration intermediate between the previous two at approximately 10 Myr (figure 3). Below, we start by presenting the evolution of the reference model (RM) and later outline the outcomes of the remaining models in relation to the RM case and, subsequently, to one another.

3.1 Reference model time evolution

The reference model has the same initial geometry as the model setup, but it does not contain an SLL (figure 1). The slab average dip-angle is approximately 70°. It slightly increases when the slab tip interacts with the bottom of the modelled box at ∼7.8 million years, after which the slab lies flat in a convex -s-shape at the 660 km discontinuity. Slab subduction into the underlying mantle is accompanied by two poloidal cells, one ahead and one behind the subducting slab (figures 2a,b). Divergence and poloidal potential values vary within ±200 Gyr and 10^{-2}–10^{-3}, respectively, for the RM case (figure 5 and6). Both are in line with the average values predicted on Earth (Bercovici, 2003; O'Connell et al., 1991). The toroidal component of the RM case is much smaller than the poloidal counterpart, and generally with $|w_z| < 7.7$ Gyr and Ψ on the order of 10^{-4} (figures 6 and 7b). Limited values of vorticity in relation to areas of high strain rates (i.e., at ridges and above the subducting slabs) may be observed, as seen in previous work (Tackley, 2000); however, this also leads to T/P ratios on the order of only a few percent. Since our RM provides a reliable base, it was chosen as a reference for comparison with models having an SLL.

3.2 Effect of SLL width on the subducting style - slab morphology and surface motions

An SLL has the overall effect of enhancing plate velocity, hampering trench retreat motion and in some cases affecting the morphology assumed by the subducting slab (figures 2 and 3), in agreement with previous work (Carluccio et al., 2019; Cerpa et al., 2022). However, in this study, the extent of these effects depends on both the viscosity contrast between SLL and the mantle ($\eta_{\mathrm{SLL}}/\eta_{\mathrm{M}}$), and the ratio between OP and SLL width (W_*). To illustrate this impact, we divide our numerical experiments into two sets. The first set, M1-M4, has moderate ($\eta_{\mathrm{SLL}}/\eta_{\mathrm{M}} = 10^2$) viscosity contrast and the second, M5-M8, has lower ($\eta_{\mathrm{SLL}}/\eta_{\mathrm{M}}$=$10^1$) viscosity contrast. For both sets, we vary W_*, from 0 to 1 with an increment of 1/4 and maintain $\eta_{\mathrm{SLL}}/\eta_{\mathrm{M}}$ constant (figure 1b).

The models within set 1 present a remarkable change in the subduction style compared to the RM (figure 2). Specifically, the M4 case ($W^* = 1$) shows the largest plate velocity with an increase up to a factor of approximately 2 compared to the RM case, continuous trench advance and a steady-state subducting slab that buckles in a concave -c- shape at the 660 km discontinuity (figures 2e,f and 3a). Subduction experiments with W_{SLL} values intermediate between the two end-member cases, RM and M4, exhibit lateral variation in the subduction style from one side to the other of the subduction zone. For example, M2 ($W^* = 0.5$), is characterised by the co-existence of two distinct slab behaviours. Specifically, the area of the slab with no SLL shows a convex -s- shape, trench retreat and a slab flattening at the 660 km boundary; conversely, the remaining part of the slab exhibits a concave -c- morphology, trench advance and a steady-state slab buckling at the transition zone (figures 2c,d and 3). Overall, we find significant lateral variation in slab morphology and surface motions for models with $1/4 \leq W_{SLL} \leq 3/4$ and smaller ones for the remaining cases (figure 3).

The second set of models presents an overall slab roll-back mechanism and trench retreat motion (figure 3). Models with $1/2 \leq W_{SLL} \leq 3/4$ show lateral variations in trench migration, but the lateral shape of the slab does not vary significantly. As such, set 2 shows reduced SLL effects compared to set 1. However, it also presents diminished trench retreat rates and enhanced plate velocities compared to the RM case (figure 3). The M8 case ($W^* = 1$) shows the highest V_P for this set of models, with an increase up to a maximum factor of $\sim$1.7 compared to the RM, and a combined quasi-stationary and retreating trench motion.

3.3 Effect of SLL width on the induced deformation flow

To summarise the impact of an SLL to the vertical and lateral transport of mass around the subducting slab, we describe end-members' behaviour for RM, M4 and M2 cases, as shown through a comparison in figures 4 and 5. In common with all the models, we observe three main characteristics: i) surface divergence is higher at ridges and above the slab (extensional areas), and smaller at the trench (i.e., at the convergence zone); ii) this trend is attenuated at the LAB; and iii) the trend reverses at deeper depths compared to the surface (figure 4). Both RM and M4 do not show lateral variation in ∇_h and share similar divergence patterns. However, M4 overall presents the largest divergence values (figure 4) justifying the model's highest plate velocity (figure 3). The same model is also characterised by a region of strong extensional flow in the sub-slab mantle due to the presence of the SLL entrained everywhere beneath the base of the oceanic plate. In M2, the inclusion of an uneven SLL causes lateral variation in the divergence field around the plane of symmetry of the subduction zone, Y=0, due to the development of a toroidal flow (figures 4 and 5h).

The comparison of the vorticity field of RM, M4 and M2 modelling cases is shown in figure 5. This comparison allows us to test that there is no substantial vorticity in models with no lateral viscosity variations regardless of depth, such as RM and M4. Conversely, it is possible to observe the development of a strong toroidal cell at the base of the oceanic lithosphere, which influences the whole model domain in M2 (figure 5, third column).

3.4 Temporal variation of the induced mantle flow and its partitioning

In our models, the strength and intensity of both the poloidal and toroidal potentials may vary during the subduction process. Their evolution through time is shown in figure 6 through a comparison among the RM, M4 and M2 cases. All these models share a few characteristics in common. Firstly, the poloidal component is active since the early stages of the slab dynamic evolution (figure 6a, c, e). Secondly, lower values of poloidal potential are registered closer to the LAB and larger ones near the base of the model, except for the initial 2 Myr where the amplitude of poloidal potential is greater nearer the surface. After this initial period, Φ is greater at lower depths due to the larger vertical motions (meaning that the slab is subducting under the weight of its own negative buoyancy), whereas closer to the base of the modelled box, it follows the trend in plate speed (figure 3).

A point of difference across these models is the trend in the temporal evolution of the poloidal potential near the LAB after the first 3 Myr. At this depth, Φ remains generally stable and does not vary significantly for the RM case. Conversely, it decreases more slowly before slightly increasing again at 8 Myr for the SLL cases. For the latter models, the changes in the evolution of poloidal potential result from SLL entrainment; the flow field evolution remains otherwise stable for the RM case. In addition, the overall highest poloidal potentials are observed for M4, followed by M2 and RM cases, resembling the hierarchy in plate velocities (figure 3).

The toroidal potentials of the RM and M4 cases are of the order of 10^{-4}, stable through time (figure 6b,d). Contrarily, for the M2 case, average values of Ψ are on the order of 10^{-3}–10^{-2}, stronger in the sub-lithosphere and deeper upper mantle where they resemble the trend evolution of the subduction speed, with lower values closer to the surface where they slightly increase over time.

3.5 Surface flow field partitioning

The comparison of the evolution of the surface flow field partitioning (T/P) through time for simulation sets 1 and 2 is shown in figures 7a and b, respectively. For the RM, M4 and M8 modelling cases, the T/P is only a few percent (2–5) and smaller compared to models with $0 < W_{SLL} < 1$, where significant toroidal flow (18–52) is found. For the latter cases, T/P generally increases with time, in particular, after the slab tip interacted with the upper-lower mantle discontinuity, at approximately 7 Myr and 8 Myr for sets 1 and 2, respectively. The first modelling set shows higher T/P values than the second due to the higher viscosity contrast SLL-UM. For the former, T/P can increase up to a maximum of 0.52 after 7 Myr and is overall stable before then with mean values ~ 0.25 (figure 7a). For the latter case, T/P exhibits reduced variability over time, with a maximum of ~ 0.2 (figure 7b).

In figure 8a, we present an additional comparison of the evolution of mantle flow for RM, M2 and M10 cases. The M10 modelling setup is the same as the RM, but its plate width is only half of the modelled box width ($W_{OP} = 1/2W_{Box}$), and as such the initial condition includes a slab free edge surrounded by mantle material. For the M10 case, the surface T/P can reach values greater than 0.8, which are not generally found in a no-net reference frame. The temporal evolution of the poloidal potential of the M10 case follows a similar trend as the other models (figures 6 and 8b), though with a lower magnitude due to its narrower slab width. However, differences arise in the M10 temporal evolution of the toroidal potential, which trend mirrors the three stages of slab speed evolution consistent across the entire model domain including at the surface where an additional toroidal cell is present (figure 8c and supporting figure 2).

3.6 The influence of sub-lithospheric layer width on the partitioning of the induced mantle flow and surface motions

The influence of SLL width on the partitioning of the induced mantle flow, T/P, surface motions ,V_T/V_P, and slab morphology is summarised in figure 9a. Models having $1/4W_{OP} < W_{SLL} < 3/4W_{OP}$ generate the most significant lateral variability in subducting slab morphology, trench migration, as well as larger values of T/P. From the analysis of the flow field partitioning emerges that the poloidal flow is the predominant component for all the models, except for when it is compared to the toroidal potential underneath the slab for SLL models having $1/4W_{OP} < W_{SLL} < 3/4W_{OP}$. For these models, the largest T/P is recorded around the LAB, followed by the deeper mantle and then the surface, with values up to 1.75 and 0.5 closer to the LAB and 660 km discontinuity, respectively (figure 8a). By applying polynomial regression, we find an empirical quadratic relationship relating T/P to W^* at different depths (figure 8). This relationship highlights that T/P is the highest when SLL extension is half of the plate width and diminishes gradually on either side by increasing or decreasing W^*. We also find an empirical linear relationship that describes the influence of W^* on the partitioning of the subduction surface motion in trench and plate migration rates (figure 8). This relationship can be used to estimate the full extent to which SLL width and viscosity parameters may affect the subduction partitioning given our particular model set-up.

3.7 Application to natural subduction zones

Our numerical simulations employ varied parameters over a range that is Earth-like applicable (figure 1b and supporting table T1) following previous work (Carluccio et al., 2019).

To test the applicability of our numerical experiments to natural subduction settings, we use the estimates on V_P and V_T from Clennett et al. (2020) relative to the mantle reference frame using the optimised plate boundary model of Tetley et al. (2019) built in a no-net reference frame for major subduction zones on Earth. The values of V_P and V_T from our models most positively align with the observed present-day plate and trench migration rates constrained within $V_T \pm 1/3V_P$ (figure 9b), which represent most subduction zones on Earth across various reference frames (Coltice et al., 2017). However, along some of the subducting segments of the Pacific rim, there is little correlation with our models (i.e., where $V_T > \pm 1/3V_P$), such as the Tonga and New Hebrides trenches. Nevertheless, many of the remaining subduction regions fall within the range of $V_T \leq \pm 1/3V_P$, while also undergoing significant lateral changes in slab morphology and trench migration, as observed in regions like Mariana, Izu-Bonin, and Nazca where an SLL has also been imaged by geophysical studies (e.g., Kawakatsu et al., 2009; Naif et al., 2013). Furthermore, we apply linear regression to all SLL models obtained in this study and find a striking linear relationship relating plate and trench migration rates. Lastly, our 3D results have been plotted on top of the 2D values obtained in the study of Carluccio et al. (2019) (in black), showing that an SLL maintains a constant signature.

4 Discussion and concluding remarks

A range of geophysical studies (e.g., Kawakatsu et al., 2009; Naif et al., 2013; Hawley et al., 2016) has recently brought considerable attention to the detailed structure of the asthenosphere at subduction zones. These studies report that asthenospheric local and regional configurations may lead to up to a $\sim$4 orders of magnitude melt-induced viscosity reduction localised into one or multiple thin and more buoyant layers at the base of the lithosphere. Such ultra-low viscosity reductions appear compatible with global plates and seismic anisotropy models as long as their lateral extent remains limited compared to the rest of the tectonic plate (Becker, 2017). However, little is known about the lateral extent of these features due to several challenges including the non-uniqueness associated with the viscosity and thickness of deep Earth layers, the elusive nature of the LAB, as well as the trade-off between the power of geophysical methods and their lateral coverage (Fischer et al., 2010; Long, 2013; Richards and Lenardic, 2018). As a consequence, thin and narrow sub-lithospheric layers have remained “hidden” from many geophysical studies and their three-dimensional impact on subduction dynamics is poorly studied.

Our numerical models address the geodynamic impact of combined SSL width and viscosity properties on the partitioning of subduction surface motions, induced mantle circulation and slab morphology. We use the plate and trench migration rates and slab morphology to characterise the subduction style in addition to using the vertical and lateral components of the flow field, their poloidal and toroidal potentials as well as their ratio to analyse the subduction-induced mantle flow.

In our study, the primary effect of introducing an SLL of a limited extent compared to the oceanic plate is to promote the development of substantial toroidal flow beneath the base of the oceanic plate, which may impact trench and plate migrations, and the morphology assumed by the subducting slab unevenly (figures 2 and 9). These effects are particularly significant for $1/4W_{OP} \leq W_{SLL} < 3/4W_{OP}$ and $\eta_{\mathrm{UM}}/\eta_{\mathrm{SLL}} \geq 10^1$, and reduced for smaller width or viscosity contrasts.

The M4 case with $W_{SLL} > 3/4W_{OP}$ and $\eta_{\mathrm{M}}/\eta_{\mathrm{SLL}}=10^2$ shows the largest plate velocities, trench advance and a steady-state subducting slab continuously buckling at the 660 km discontinuity. Subduction experiments with $1/4W_{OP} \leq W_{SLL} < 3/4W_{OP}$ exhibit large plate speed, changes in slab morphology (s-to-c shape) and trench migration (retreat to advance) from one side to the other of the subduction zone (figures 2 and 3). Models with reduced SLL width ($W_{SLL} \leq 1/4W_{OP}$) and/or viscosity contrast ($\eta_{\mathrm{M}}/\eta_{\mathrm{SLL}} < 10^2$) show overall smaller lateral variations in trench and plate migration rates and slab behaviours.

We find that combined SLL width and viscosity variations enhance an overall advancing trend for both plate and trench motions, in addition to increasing V_P up to a factor of ~ 2. However, they have only a limited effect on slab tip migration (figure 3c, f); thus, showing once again that an SLL has a greater influence on tangential motions than it has on vertical movements, consistent with previous findings (Carluccio et al., 2019). Viscosity reductions at the base of the lithosphere can result in the entrainment of an SLL (e.g., Kawakatsu et al., 2009; Hawley et al., 2016). By reducing the viscous drag on one of the slab sides, an SLL favours the gravitational sliding of the oceanic plate justifying the increase in slab velocity up to a factor of two observed in our models. The slab dynamic behaviour is then driven by both slab pull and asthenospheric drag exerted at the base of the plate opposed by the viscous flow induced by the adjacent mantle and the slab bending resistance (e.g., Ribe, 2001; Capitanio et al., 2007; Natarov and Conrad, 2012; Coltice et al., 2019).

In accordance with previous work (e.g., Funiciello et al., 2004; Stegman et al., 2006; Piromallo et al., 2006; Capitanio and Faccenda, 2012), we find the subduction-induced mantle flow to be highly three-dimensional where poloidal and toroidal flows coexist since the early stage of subduction. In our models, poloidal motion represents the predominant flow component at the surface (figure 9a). Consistent with previous work (Holt et al., 2017), we also find that the amplitude of the toroidal:poloidal ratio is greater in the mantle compared to the surface (figure 9).

Significant T/P (20-60%) is only found in models having lateral viscosity variations, such as $0 < W^* < 1$, and is due to the development of a toroidal cell beneath the base of the lithosphere (figure 5). These models record T/P values that are one order of magnitude greater than what is found in the other cases ($W^* = 0, 1$), where this ratio is otherwise on the order of only a few percent (2-7%) and stable over time. Models showing considerable toroidal flow are characterised by T/P that generally increases over time and, specifically, after the slab tip has interacted with the upper-lower mantle transition zone at approximately 7 Myr and 8 Myr for sets 1 and 2, respectively. For simulation set 1, the maximum observed surface T/P is 0.52 and approximately 0.2 prior to 7 Myr. Conversely, the second set of models presents lower T/P variability over time with a maximum value of $\sim$0.2.

Sub-lithospheric lateral viscosity and width variations induce lateral flow migration and the development of toroidal flow patterns. We attribute the increase in T/P through time to the presence of an entrained SLL beneath the slab. By acting as a partial barrier, an SLL compels mantle flow to migrate laterally generating a toroidal cell underneath the base of the lithosphere (figures 2 and 5). Lateral flow migration is further enhanced by the slab sinking into the mantle through time, which provides an additional physical barrier to mantle flow in the trench-strike direction. The combined action of these two mechanisms strengthens the amplitude of the toroidal component more than its poloidal counterpart over time (figure 6), resulting in an increase in T/P, as well as in uneven lateral patterns of trench migration and slab morphology (figures 2 and 3).

Our study shows that variations in SLL width and viscosity can induce significant vorticity from buoyancy-driven convection leading to Earth-like T/P values, which had proven difficult with previous generations of subduction numerical studies with a continuous slab. These outcomes provide an alternative and novel mechanism for the apparent lack of a direct link between the slab pull driving force in buoyant convection and the generation of toroidal flow; thus showing that substantial toroidal flow can be induced from a buoyancy-driven flow by introducing horizontal viscosity variations within the top asthenosphere (Tackley, 2000; Bercovici, 2003).

Furthermore, we identify an empirical second-order relationship that describes T/P and the subduction style as a function of W^*. This relationship indicates that the largest T/P are found for the most asymmetric cases, such as M2, characterised by the co-occurrence of a c-to-s slab shape and retreat-to-advance trench motion. The toroidal:poloidal ratio and asymmetry in the subduction style diminish gradually by either decreasing or increasing W^* reflecting in the prevalence of either s or c slab morphology, and retreating or advancing trench migration, respectively (figure 9).

Our models develop T/P values that fall within the observed surface range of 0.2-0.5, consistent with what would be expected in a no-net reference frame (Bercovici, 2003). Similarly, our average vorticity and divergence values (± 200 Gyr^{-1}) align closely with the present-day surface flow field data obtained through the analytical NUVEL-1 model by O'Connell et al. (1991). Our subduction partitioning values also fall within $\pm 1/3$, consistent with observations for most natural subduction zones regardless of the reference frame adopted (Coltice et al., 2017).

Our findings outline a means to aid the interpretation of the geological record of subduction zones characterised by lateral variations in the subduction style (e.g., uneven plate speed, trench migration as well as convex-to-concave slab shape) and mantle flow patterns (e.g., trench parallel-to-perpendicular anisotropy), as observed in Izu-Bonin, Hikurangi-Kermadec, and Nazca regions, among others (Long, 2013; Goes et al., 2017). In these regions, geophysical studies (Naif et al., 2013; Stern et al., 2015; Kawakatsu et al., 2009) have imaged the presence of an SLL, and if it is indeed present, it could help to explain some of the intricacies in the patterns of slab and mantle deformation observed in these natural systems. However, in certain subduction zones, like those along the margins of Tonga and New Hebrides trenches, there is little correlation with our models, indicated by V_T values exceeding $\pm 1/3 V_P$. While we do not exclude that other mechanisms could hold significant importance or coexist with the presence of an SLL (e.g., double subduction systems, arcuate arcs), yet an SLL would be expected to play a crucial role in the partitioning of surface- and deep-induced motions, as well as broader subduction dynamics, highlighting the importance of these geological features emerging from various geophysical studies.

Nonetheless, we also perform a small number of additional numerical experiments to explore the extent to which our approach may influence our conclusions. We tested the role of the lower mantle (supporting figure 1) and that of a slab-free edge setup often used in numerical studies (figure 8). While the choice of parameters can be different, an SLL continues to maintain a consistent signature. Additionally, we find that a slab-free edge setup develops T/P pick values of 0.8, which are not estimated in a no-net reference frame. Based on the differences and similarities between M10 and our other models, our results indicate that slab-free edge models can be used to describe slab vertical motion and dynamics, but they may not comprehensively capture lateral flow dynamics.

Previous numerical work has provided useful insights towards the modelling of three-dimensional flow associated with the subduction of an oceanic lithosphere into the mantle. Several studies (e.g., Conrad and Hager, 1999; Funiciello et al., 2004; Schellart et al., 2007; Stegman et al., 2006; Kincaid and Griffiths, 2003, 2004; Kneller and Van Keken, 2008; Piromallo et al., 2006; Goes et al., 2011; Gérault et al., 2012; Faccenda and Capitanio, 2012; Király et al., 2017) have documented mantle flow patterns around a slab edge induced by trench migration, slab and mantle properties contrast, rheology, temperature distribution around the slab, plate age and strength, lateral variations in plate and trench widths, ridge position and plate coupling at the trench zone. Yet, these studies have not explored the influence of an SLL on the partitioning of the induced mantle flow and surface motions. For the first time, we have explored this impact in light of the recent observations (e.g., Kawakatsu et al., 2009; Naif et al., 2013; Hawley et al., 2016) of a decoupling SLL beneath the base of a subducting zone in a 3D fashion.

Our study reveals that regional SLL width and viscosity variations promote the development of laterally varying patterns in plate and trench motions, induced mantle flow and slab morphology. As importantly, the presence of a non-uniform regional SLL in a free single-slab subduction model itself is significant in generating a substantial source of toroidal flow (figure 9a) and aligns more closely with the average values presently estimated on Earth in a no-net reference frame (0.2-0.6), which had proven challenging to achieve in previous generations of numerical models (Tackley, 2000; Bercovici, 2003). This regional SLL mechanism may have important consequences for global subduction dynamics, including back-arc formation and melt and volatile transport around the subducting slab. Furthermore, this mechanism could enhance our understanding of lithosphere-mantle processes and our understanding of lithosphere-mantle processes and contribute valuable insights into the evolutionary dynamics of mantle circulation over geological time.

Credit authorship contribution statement

Roberta Carluccio: Conceptualization, Data curation, Formal analysis, Investigation, Visualization, Funding acquisition, Writing – Editing, Writing – original draft. Louis Moresi: Conceptualization, Funding acquisition, Supervision, Editing. Fabio Capitanio: Conceptualization, Supervision, Editing. Rebecca Farrington: Conceptualization, Funding acquisition, Supervision. Lorenzo Colli: Investigation, Validation, Editing. Ben Mather: Data curation.

Declaration of Competing Interest

The authors declare that they have no known competing financial interests or personal relationships that could have appeared to influence the work reported in this paper.

Data availability

The software and code are open sources. We provide the https://zenodo.org/records/5935717 of the 2.12.0b version of the Underworld2 code used in this study. Linear and nonlinear regression, and multivariate regression analysis Jupyter Notebooks are available online https://github.com/rcarluccio/MachineLearningApplications.

Acknowledgements

The authors are grateful to J. Mansour and other colleagues at the University of Melbourne for their constructive comments and suggestions. The research was supported by the Australian Research Council Discovery Project grant (DP150102887), the David Hay Postgraduate Writing Up Award (University of Melbourne) and the Laura Bassi scholarship. The computations were performed by using the NCI supercomputer Gadi with the use of the Adapter Scheme, NCMAS and Sydney Informatics Hub (SIH) national computing grants and funds. Users can access data from this paper by contacting the authors.

References

D. L. Anderson. Lithosphere, asthenosphere, and perisphere. *Reviews of Geophysics*, 33(1):125–149, 1995.

T. W. Becker. Superweak asthenosphere in light of upper mantle seismic anisotropy. *Geochemistry, Geophysics, Geosystems*, 18(5):1986–2003, 2017. ISSN 15252027. doi: 10.1002/2017GC006886. https://doi.org/10.1002/2017GC006886.

D. Bercovici. The generation of plate tectonics from mantle convection. *Earth and Planetary Science Letters*, 205(3):107–121, 2003.

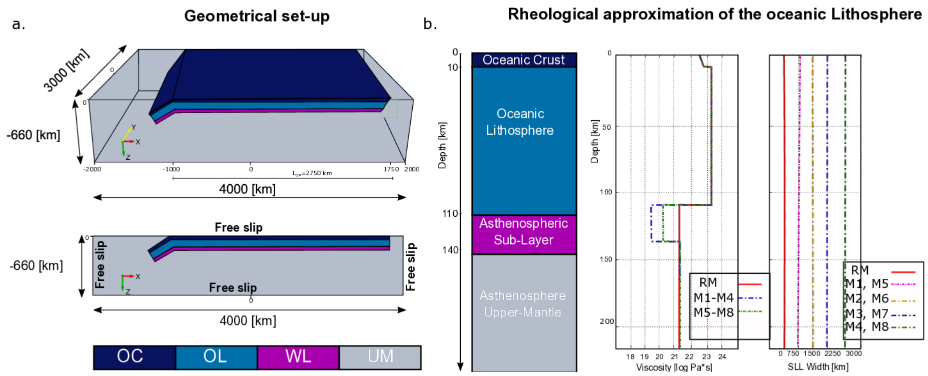

Figure 1: In a, a simplified representation of the geometrical setup with a sub-lithospheric layer (SLL). In b, the material field (first column) and the initial viscosity (mid-column) profiles through depth for simulation sets 1 (RM, M1-M4) and 2 (M5-M8). The final columns provide information about SLL width for the two sets.

D. Bercovici and P. Wessel. A continuous kinematic model of plate-tectonic motions. *Geophysical Journal International*, 119(2):595–610, 1994.

D. Bercovici, P. Tackley, and Y. Ricard. The generation of plate tectonics from mantle dynamics. In *Treatise on Geophysics*, volume 7.07, pages 271–318. Elsevier, Oxford, 2015.

M. I. Billen and G. Hirth. Newtonian versus non-newtonian upper mantle viscosity: Implications for subduction initiation. *Geophysical Research Letters*, 32(19), 2005. https://doi.org/10.1029/2005GL023457.

G. Bokelmann. Which forces drive north america? *Geology*, 30(11):1027–1030, 2002.

O. Čadek and Y. Ricard. Toroidal/poloidal energy partitioning and global lithospheric rotation during cenozoic time. *Earth and Planetary Science Letters*, 109(3-4):621–632, 1992.

F. Capitanio, G. Morra, and S. Goes. Dynamic models of downgoing plate-buoyancy driven subduction: Subduction motions and energy dissipation. *Earth and Planetary Science Letters*, 262(1-2):284–297, 2007.

F. A. Capitanio and M. Faccenda. Complex mantle flow around heterogeneous subducting oceanic plates. *Earth and Planetary Science Letters*, 353:29–37, 2012.

R. Carluccio, B. Kaus, F. Capitanio, and L. Moresi. The impact of a very weak and thin upper asthenosphere on subduction motions. *Geophysical Research Letters*, 46(21):11893–11905, 2019.

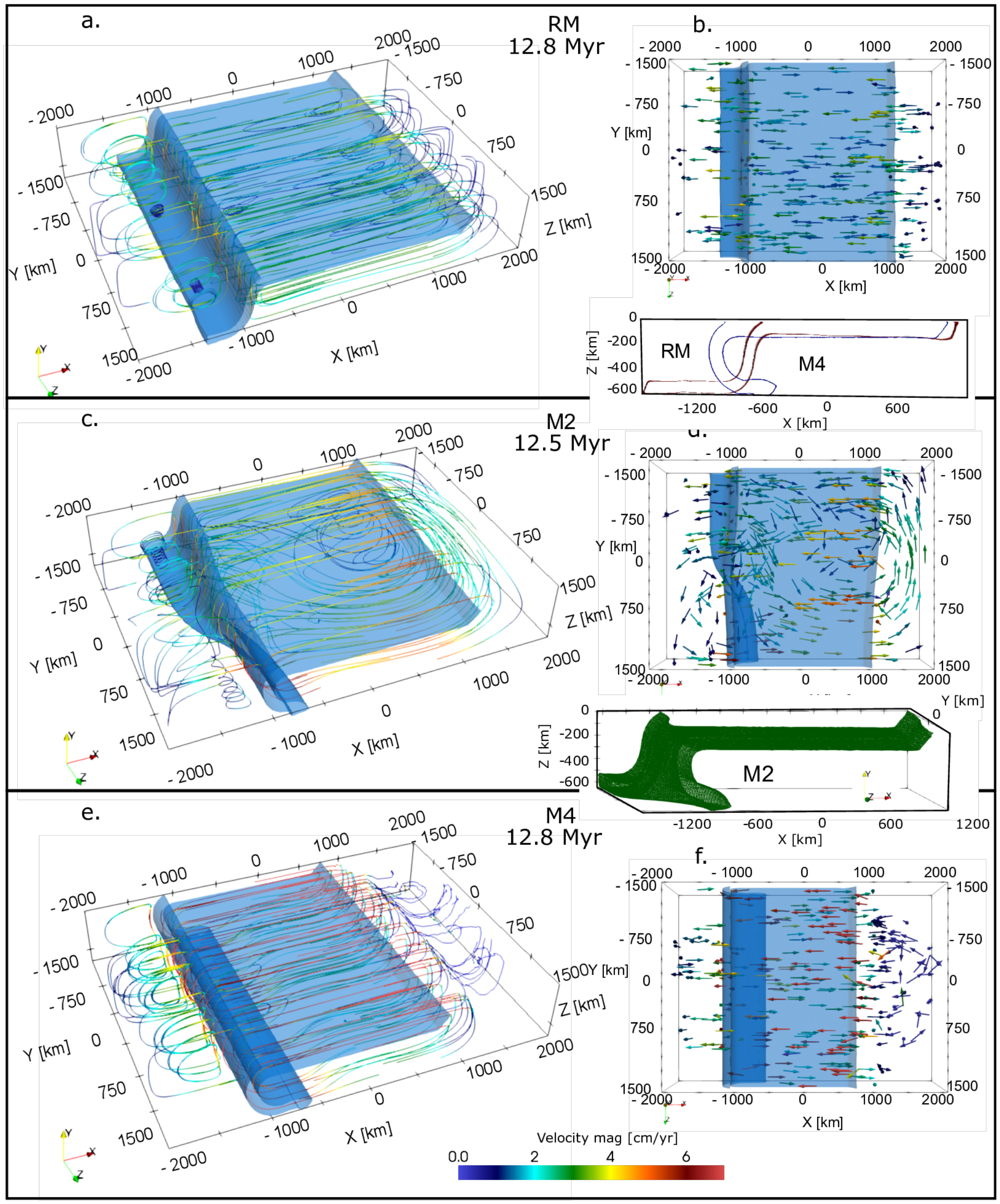

Figure 2: Subduction style comparison (from top to bottom) the RM ($\eta_{\mathrm{SLL}}/\eta_{\mathrm{M}}$=$10^0$ and $W_{SLL} = 0$), M2 ($\eta_{\mathrm{SLL}}/\eta_{\mathrm{M}}$=$10^2$ and $W_{SLL} = 1/2W_{OP}$) and M4 ($\eta_{\mathrm{SLL}}/\eta_{\mathrm{M}}$=$10^2$ with $W_{SLL} = W_{OP}$) at the steady-state stage of the time evolution. Non-planar and planar views are shown in the left and right columns, respectively, including a comparison of the subduction style for the three end-members' models. The streamline indicate flow pattern and direction of flow, and the magnitude of the subduction velocity.

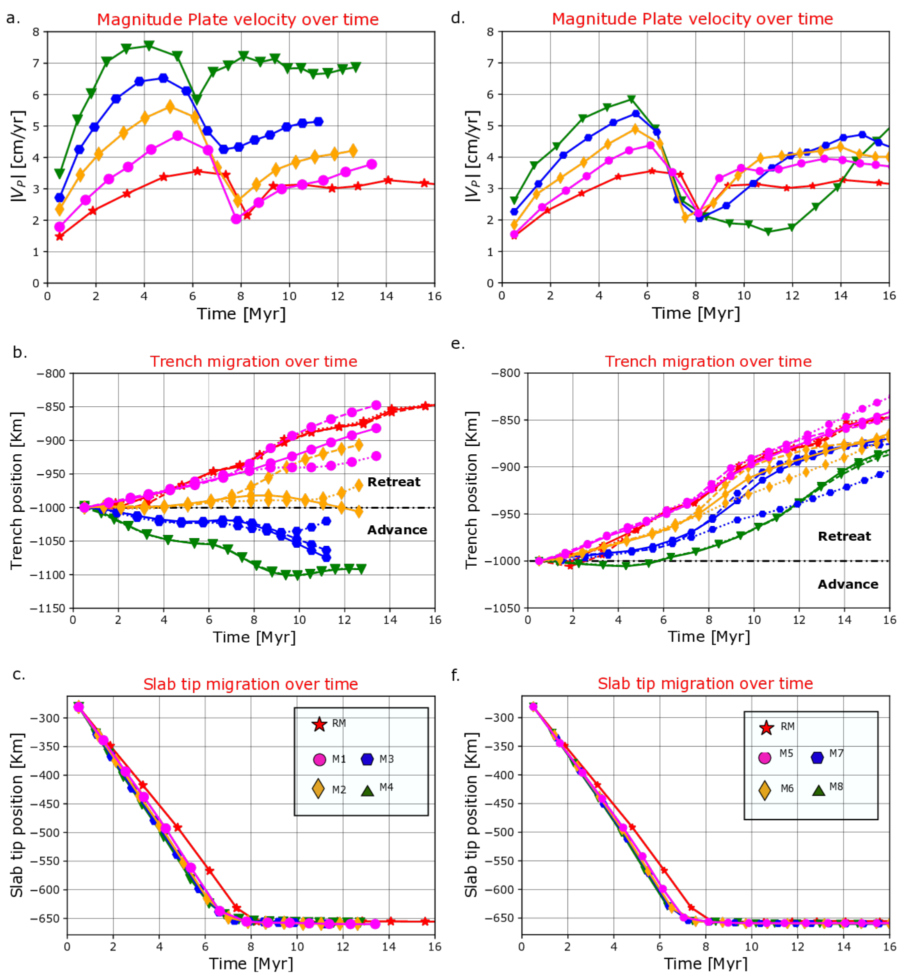

Figure 3: Evolution of plate velocities (V_P), trench and slab tip migrations through time, for simulation sets 1 and 2 in a, b, c and d, e, f, respectively.

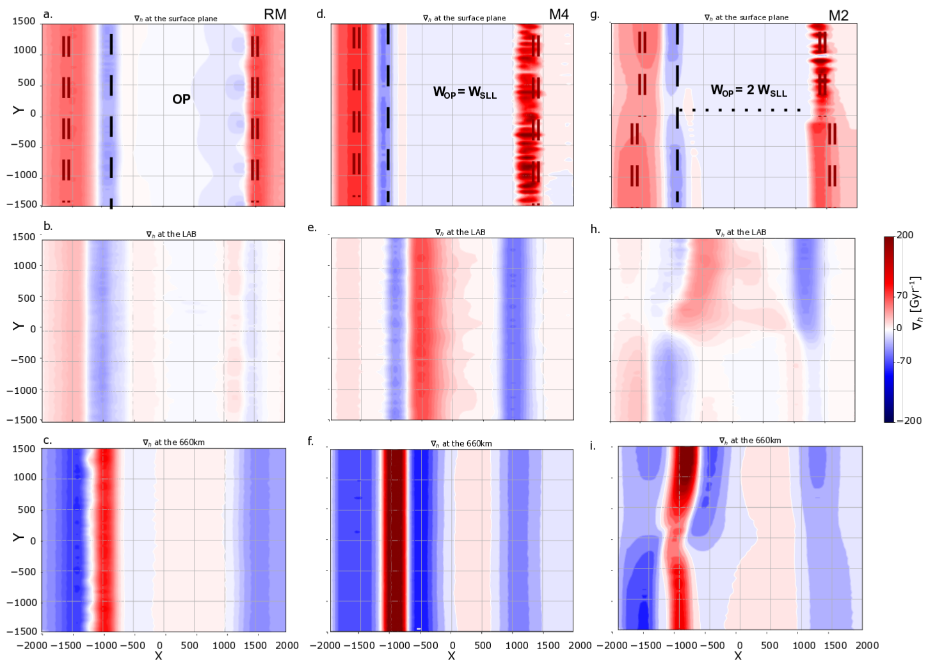

Figure 4: Horizontal divergence fields (left to right) for the RM, M4, and M2 in the proximity of (top to bottom) the surface (a, d, g), lithosphere-asthenosphere boundary (b, e, h) and 660 km bottom boundary of the model (c, f, i).

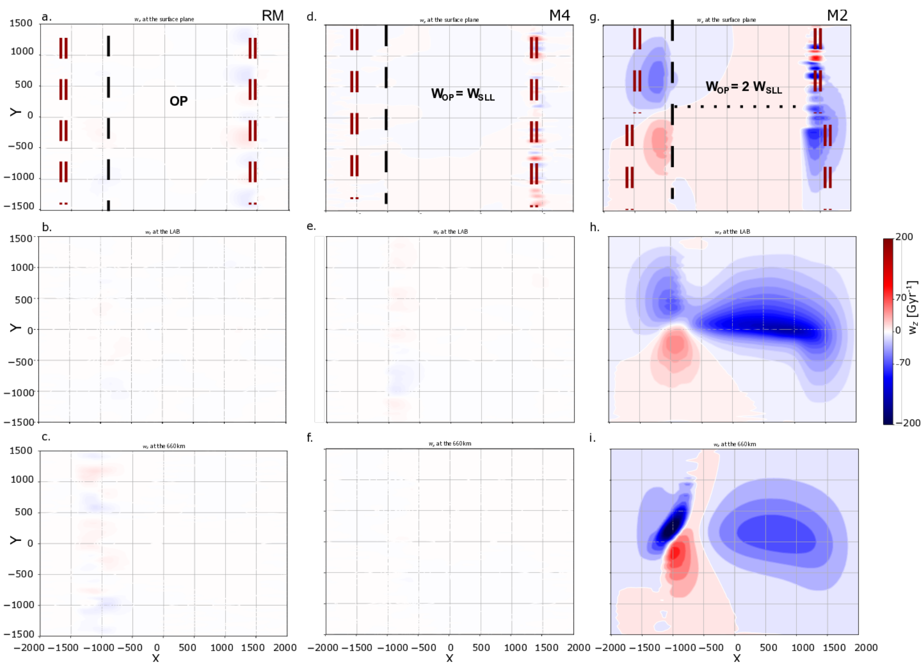

Figure 5: Radial vorticity fields (left to right) for the RM, M4, and M2 in the proximity of (top to bottom) the surface (a, d, g), lithosphere-asthenosphere boundary (b, e, h) and 660 km bottom boundary of the model (c, f, i).

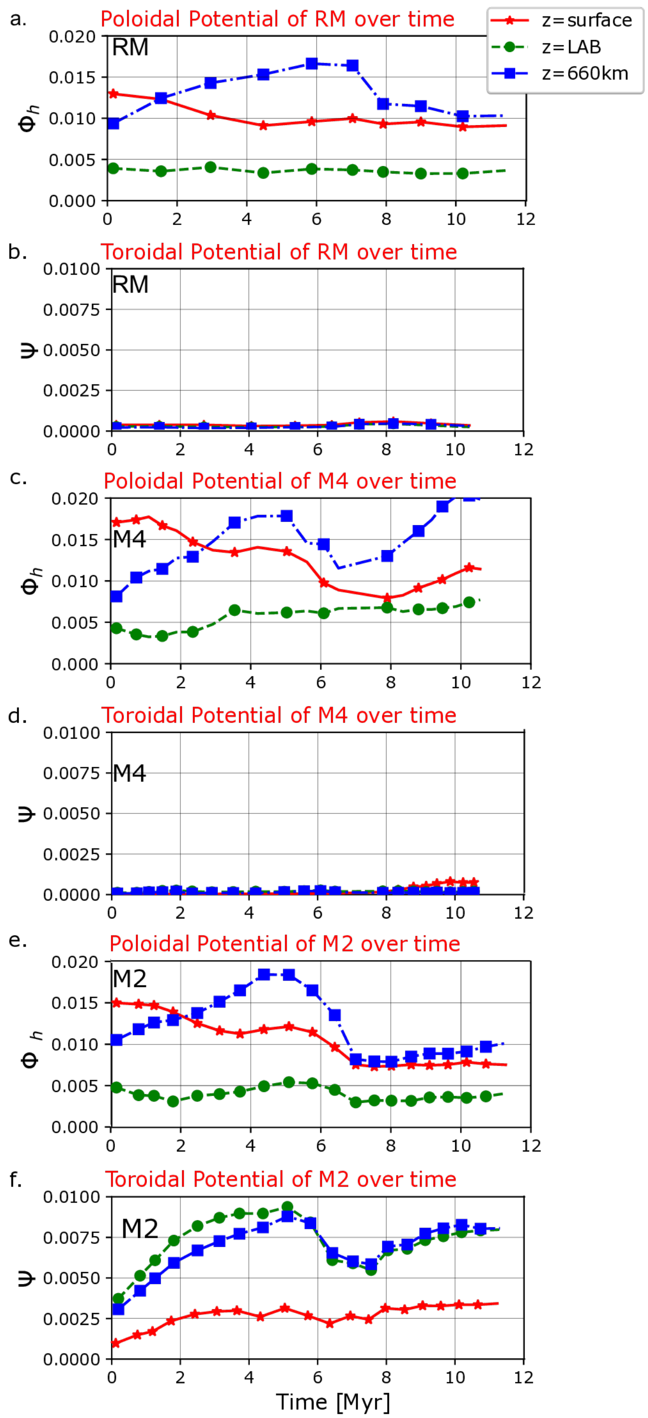

Figure 6: A comparison between the time evolution of the poloidal potential, Φ, and the toroidal potential, Ψ, for the RM, M4, and M2 cases at three different XY cross-sections through depth (i.e., surface, LAB, and 660 km depths in red, green, and blue, respectively).

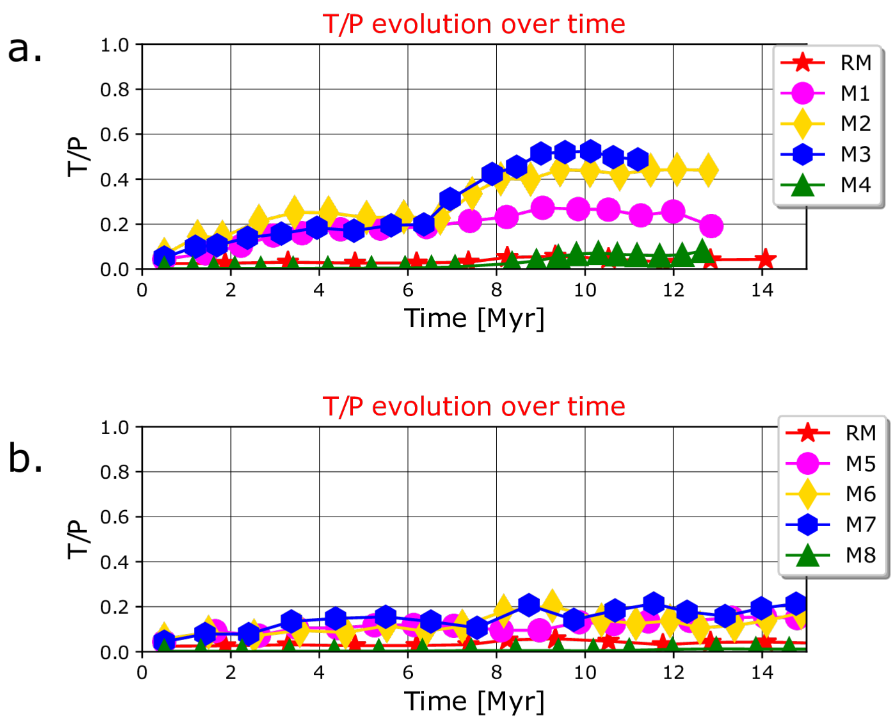

Figure 7: A comparison between the time evolution of the partitioning of induced mantle flow (T/P) for simulation sets 1 and 2, in a and b, respectively.

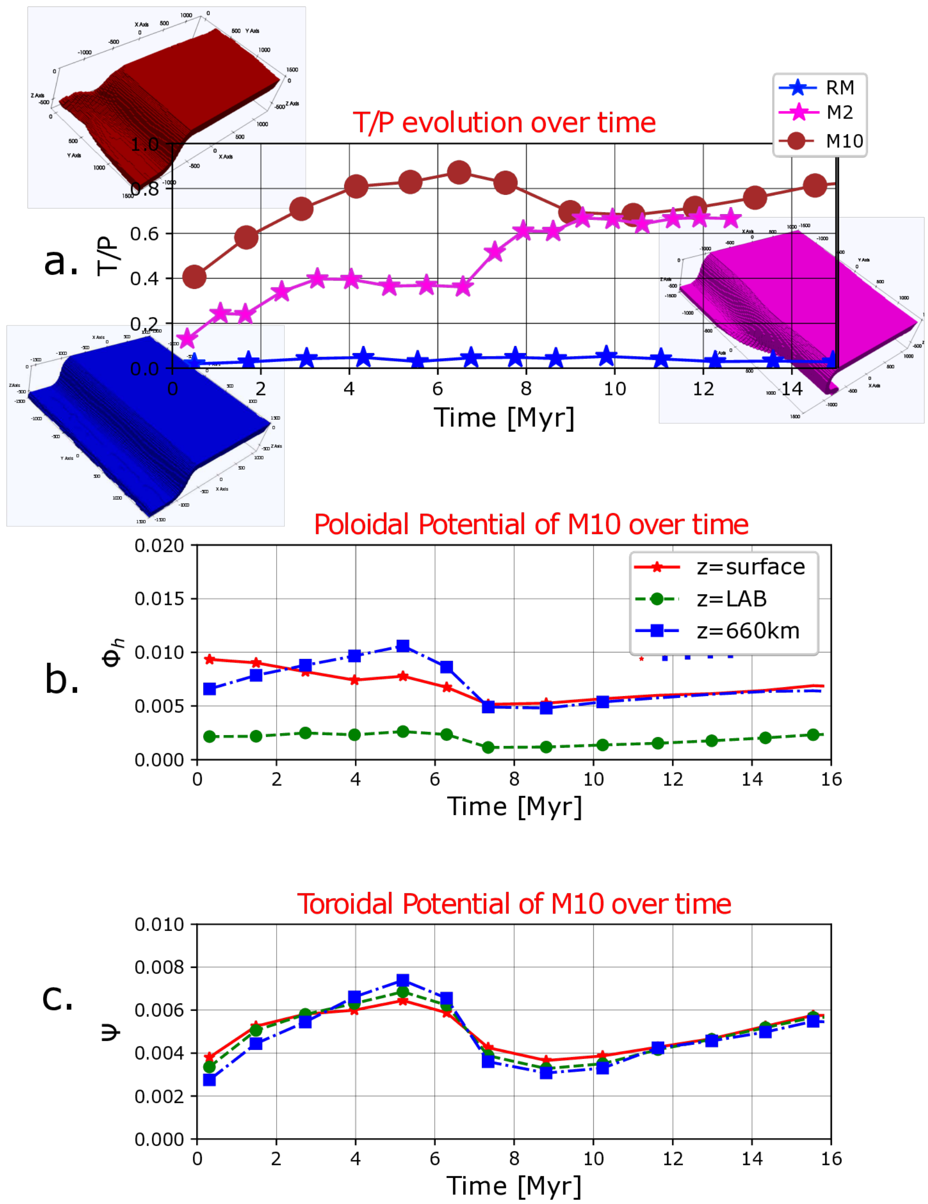

Figure 8: In a, a comparison of T/P time evolution for the RM, M2 case, and the slab free-edge model, M10. The time evolution of Φ_h and Ψ for M10 are shown in b and c, respectively.

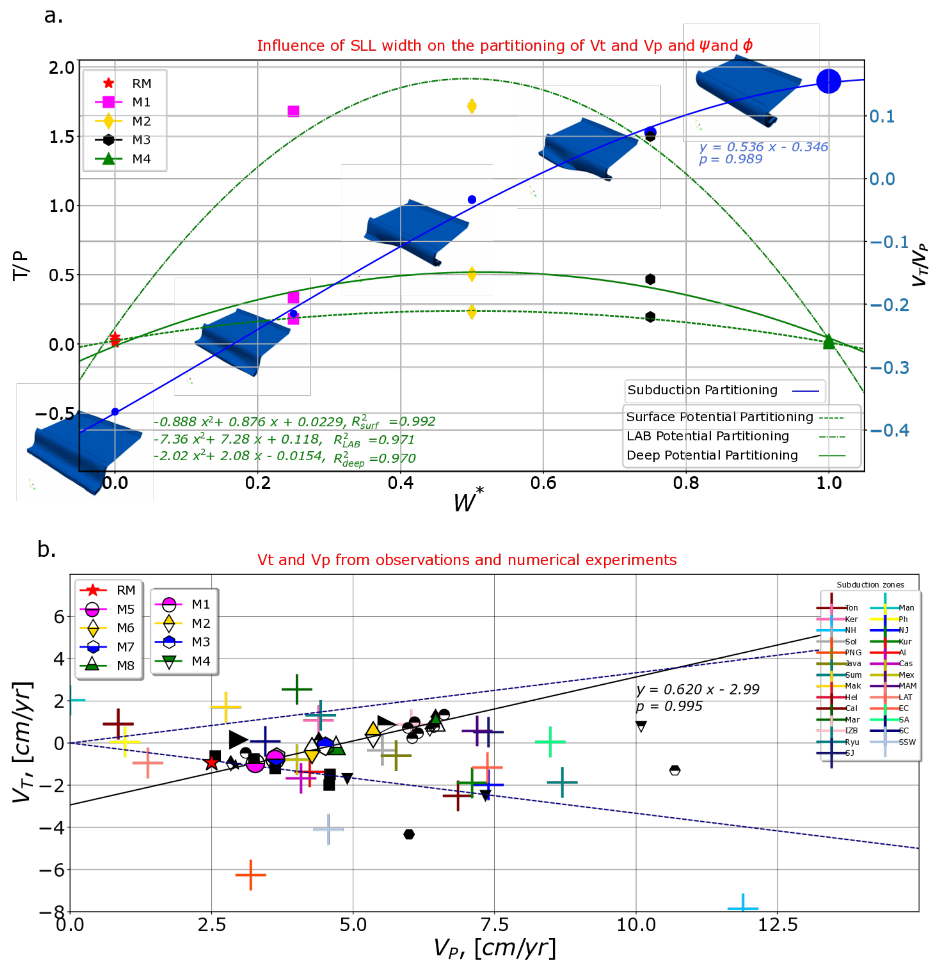

Figure 9: In a, a summary of the influence of SLL-OP width ratios ($W^* = W_{SLL}/W_{OP}$) on T/P, surface motions partitioning (V_T/V_P) and the subduction style. A second- and first-order empirical relationships relating W^* to T/P and V_T/V_P are identified. In b, the relationship between V_P and trench velocity V_T, as found in our 3D experiments (coloured polygons), in the 2D experiments of Carluccio et al. (2019) (black polygons), and in natural cases (Clennett et al., 2020) in coloured crosses. Simulations with an SLL have a half-filled marker style, which is full otherwise. Most of the numerical and natural data lie between the dotted lines (V_T=mV_P) having m equal to ±1/3, which includes the majority of natural subduction zones across various reference frames. The 3D models containing an SLL lie on a straight line with a Pearson coefficient of 0.998.

N. G. Cerpa, K. Sigloch, F. Garel, A. Heuret, D. R. Davies, and M. G. Mihalynuk. The effect of a weak asthenospheric layer on surface kinematics, subduction dynamics and slab morphology in the lower mantle. *Journal of Geophysical Research: Solid Earth*, 127(8):e2022JB024494, 2022.

U. Christensen and H. Harder. 3-d convection with variable viscosity. *Geophysical Journal International*, 104(1):213–226, 1991.

E. J. Clennett, K. Sigloch, M. G. Mihalynuk, M. Seton, M. A. Henderson, K. Hosseini, A. Mohammadzaheri, S. T. Johnston, and R. D. Müller. A quantitative tomotectonic plate reconstruction of western north america and the eastern pacific basin. *Geochemistry, Geophysics, Geosystems*, 21(8): e2020GC009117, 2020.

M. Cloos. Lithospheric buoyancy and collisional orogenesis: Subduction of oceanic plateaus, continental margins, island arcs, spreading ridges, and seamounts. *Geological Society of America Bulletin*, 105(6):715–737, 1993.

N. Coltice, M. Gérault, and M. Ulvrová. A mantle convection perspective on global tectonics. *Earth-Science Reviews*, 165:120–150, 2017. ISSN 00128252. doi: 10.1016/j.earscirev.2016.11.006. https://doi.org/10.1016/j.earscirev.2016.11.006.

N. Coltice, L. Husson, C. Faccenna, and M. Arnould. What drives tectonic plates? *Science Advances*, 5(10):eaax4295, 2019. https://doi.org/10.1126/sciadv.aax4295.

C. P. Conrad and B. H. Hager. Effects of plate bending and fault strength at subduction zones on plate dynamics. *Journal of Geophysical Research: Solid Earth*, 104(B8):17551–17571, 1999.

C. P. Conrad and C. Lithgow-Bertelloni. How mantle slabs drive plate tectonics. *Science*, 298(5591):207–209, 2002.

F. Crameri and P. J. Tackley. Spontaneous development of arcuate single-sided subduction in global 3-d mantle convection models with a free surface. *Journal of Geophysical Research: Solid Earth*, 119(7):5921–5942, 2014.

M. Faccenda and F. A. Capitanio. Development of mantle seismic anisotropy during subduction-induced 3-d flow. *Geophysical Research Letters*, 39(11), 2012. https://doi.org/10.1029/2012GL051988.

C. Faccenna, T. W. Becker, S. Lallemand, Y. Lagabrielle, F. Funiciello, and C. Piromallo. Subduction-triggered magmatic pulses: A new class of plumes? *Earth and Planetary Science Letters*, 299(1-2):54–68, 2010.

K. M. Fischer, H. A. Ford, D. L. Abt, and C. A. Rychert. The lithosphere-asthenosphere boundary. *Annual Review of Earth and Planetary Sciences*, 38:551–575, 2010.

D. Forsyth et al. On the relative importance of the driving forces of plate motion. *Geophysical Journal International*, 43(1):163–200, 1975.

F. Funiciello, C. Faccenna, D. Giardini, and K. Regenauer-Lieb. Dynamics of retreating slabs: 2. insights from three-dimensional laboratory experiments. *Journal of Geophysical Research: Solid Earth*, 108(B4), 2003. https://doi.org/10.1029/2001JB000896.

F. Funiciello, C. Faccenna, and D. Giardini. Role of lateral mantle flow in the evolution of subduction systems: insights from laboratory experiments. *Geophysical Journal International*, 157(3):1393–1406, 2004.

F. Funiciello, C. Faccenna, A. Heuret, S. Lallemand, E. Di Giuseppe, and T. Becker. Trench migration, net rotation and slab–mantle coupling. *Earth and Planetary Science Letters*, 271(1):233–240, 2008.

C. W. Gable, R. J. O'connell, and B. J. Travis. Convection in three dimensions with surface plates: Generation of toroidal flow. *Journal of Geophysical Research: Solid Earth*, 96(B5):8391–8405, 1991.

M. Gérault, T. Becker, B. Kaus, C. Faccenna, L. Moresi, and L. Husson. The role of slabs and oceanic plate geometry in the net rotation of the lithosphere, trench motions, and slab return flow. *Geochemistry, Geophysics, Geosystems*, 13(4), 2012. https://doi.org/10.1029/2011GC003934.

S. Goes, F. Capitanio, G. Morra, M. Seton, and D. Giardini. Signatures of downgoing plate-buoyancy driven subduction in cenozoic plate motions. *Physics of the Earth and Planetary Interiors*, 184(1-2):1–13, 2011.

S. Goes, R. Agrusta, J. van Hunen, and F. Garel. Subduction-transition zone interaction: A review. *Geosphere*, 13(3):644–664, 2017.

B. H. Hager and R. J. O'connell. Subduction zone dip angles and flow driven by plate motion. *Tectonophysics*, 50(2-3):111–133, 1978.

W. B. Hawley, R. M. Allen, and M. A. Richards. Tomography reveals buoyant asthenosphere accumulating beneath the juan de fuca plate. *Science*, 353 (6306):1406–1408, 2016.

A. Holt, L. Royden, and T. Becker. The dynamics of double slab subduction. *Geophysical Journal International*, 209(1):250–265, 2017.

H. Kawakatsu, P. Kumar, Y. Takei, M. Shinohara, T. Kanazawa, E. Araki, and K. Suyehiro. Seismic evidence for sharp lithosphere-asthenosphere boundaries of oceanic plates. *Science*, 324(5926):499–502, 2009.

C. Kincaid and R. Griffiths. Laboratory models of the thermal evolution of the mantle during rollback subduction. *Nature*, 425(6953):58–62, 2003.

C. Kincaid and R. Griffiths. Variability in flow and temperatures within mantle subduction zones. *Geochemistry, Geophysics, Geosystems*, 5(6), 2004. https://doi.org/10.1029/2003GC000666.

Á. Király, F. A. Capitanio, F. Funiciello, and C. Faccenna. Subduction induced mantle flow: Length-scales and orientation of the toroidal cell. *Earth and Planetary Science Letters*, 479:284–297, 2017.

E. A. Kneller and P. E. Van Keken. Effect of three-dimensional slab geometry on deformation in the mantle wedge: Implications for shear wave anisotropy. *Geochemistry, Geophysics, Geosystems*, 9(1), 2008. https://doi.org/10.1029/2007GC001677.

C. Lithgow-Bertelloni and M. A. Richards. Cenozoic plate driving forces. *Geophysical Research Letters*, 22(11):1317–1320, 1995.

C. Lithgow-Bertelloni, M. A. Richards, Y. Ricard, R. J. O'Connell, and D. C. Engebretson. Toroidal-poloidal partitioning of plate motions since 120 ma. *Geophysical Research Letters*, 20(5):375–378, 1993.

M. D. Long. Constraints on subduction geodynamics from seismic anisotropy. *Reviews of Geophysics*, 51(1):76–112, 2013.

J. Mansour, J. Giordani, L. Moresi, R. Beucher, O. Kaluza, M. Velic, R. Farrington, S. Quenette, and A. Beall. Underworld2: Python geodynamics modelling for desktop, hpc and cloud. *Journal of Open Source Software*, 5(47): 1797, 2020.

A. K. McNamara, E. J. Garnero, and S. Rost. Tracking deep mantle reservoirs with ultra-low velocity zones. *Earth and Planetary Science Letters*, 299(1): 1–9, 2010.

L. Moresi and V. Solomatov. Mantle convection with a brittle lithosphere: thoughts on the global tectonics styles of the Earth and Venus. *Geophysical Journal International*, 133:669–682, 1998.

L. Moresi, S. Quenette, V. Lemiale, C. Meriaux, B. Appelbe, and H.-B. Mühlhaus. Computational approaches to studying non-linear dynamics of the crust and mantle. *Physics of the Earth and Planetary Interiors*, 163(1-4): 69–82, 2007.

L. Moresi, P. G. Betts, M. S. Miller, and R. A. Cayley. Dynamics of continental accretion. *Nature*, 508(7495):245, 2014.

S. Naif, K. Key, S. Constable, and R. Evans. Melt-rich channel observed at the lithosphere-asthenosphere boundary. *Nature*, 495(7441):356–359, 2013.

S. I. Natarov and C. P. Conrad. The role of poiseuille flow in creating depth-variation of asthenospheric shear. *Geophysical Journal International*, 190(3): 1297–1310, 2012.

P. Olson and D. Bercovici. On the equipartition of kinetic energy in plate tectonics. *Geophysical research letters*, 18(9):1751–1754, 1991.

R. J. O'Connell, C. W. Gable, and B. H. Hager. Toroidal-poloidal partitioning of lithospheric plate motions. In *Glacial Isostasy, Sea-Level and Mantle Rheology*, pages 535–551. Springer, 1991.

C. Piromallo, T. Becker, F. Funiciello, and C. Faccenna. Three-dimensional instantaneous mantle flow induced by subduction. *Geophysical Research Letters*, 33(8), 2006. https://doi.org/10.1029/2005GL025390.

A. Pusok and B. J. Kaus. Development of topography in 3-d continental-collision models. *Geochemistry, Geophysics, Geosystems*, 16(5):1378–1400, 2015.

A. E. Pusok and D. R. Stegman. Formation and stability of same-dip double subduction systems. *Journal of Geophysical Research: Solid Earth*, 124(7): 7387–7412, 2019.

A. E. Pusok, B. J. Kaus, and A. A. Popov. The effect of rheological approximations in 3-d numerical simulations of subduction and collision. *Tectonophysics*, 746:296–311, 2018.

N. Ribe. Bending and stretching of thin viscous sheets. *Journal of Fluid Mechanics*, 433:135–160, 2001.

N. M. Ribe. Seismic anisotropy and mantle flow. *Journal of Geophysical Research: Solid Earth*, 94(B4):4213–4223, 1989.

M. A. Richards and A. Lenardic. The cathles parameter (ct): A geodynamic definition of the asthenosphere and implications for the nature of plate tectonics. *Geochemistry, Geophysics, Geosystems*, 19(12):4858–4875, 2018.

W. Schellart, J. Freeman, D. Stegman, L. Moresi, and D. May. Evolution and diversity of subduction zones controlled by slab width. *Nature*, 446(7133): 308–311, 2007.

W. P. Schellart and L. Moresi. A new driving mechanism for backarc extension and backarc shortening through slab sinking induced toroidal and poloidal mantle flow: Results from dynamic subduction models with an overriding plate. *Journal of Geophysical Research: Solid Earth*, 118(6):3221–3248, 2013.

H. Schmeling, A. Babeyko, A. Enns, C. Faccenna, F. Funiciello, T. Gerya, G. Golabek, S. Grigull, B. Kaus, G. Morra, et al. A benchmark comparison of spontaneous subduction models—towards a free surface. *Physics of the Earth and Planetary Interiors*, 171(1):198–223, 2008.

B. Scoppola, D. Boccaletti, M. Bevis, E. Carminati, and C. Doglioni. The westward drift of the lithosphere: A rotational drag? *Geological Society of America Bulletin*, 118(1-2):199–209, 2006.

D. Stegman, J. Freeman, W. Schellart, L. Moresi, and D. May. Influence of trench width on subduction hinge retreat rates in 3-d models of slab rollback. *Geochemistry, Geophysics, Geosystems*, 7(3), 2006. https://doi.org/10.1029/2005GC001056.

T. Stern, S. Henrys, D. Okaya, J. Louie, M. Savage, S. Lamb, H. Sato, R. Sutherland, and T. Iwasaki. A seismic reflection image for the base of a tectonic plate. *Nature*, 518(7537):85–88, 2015.

P. Sternai, L. Jolivet, A. Menant, and T. Gerya. Driving the upper plate surface deformation by slab rollback and mantle flow. *Earth and Planetary Science Letters*, 405:110–118, 2014.

P. J. Tackley. Self-consistent generation of tectonic plates in time-dependent, three-dimensional mantle convection simulations. *Geochemistry, Geophysics, Geosystems*, 1(8), 2000. doi: 10.1029/2000GC000036. https://doi:10.1029/2000GC000036.

M. G. Tetley, S. E. Williams, M. Gurnis, N. Flament, and R. D. Müller. Constraining absolute plate motions since the triassic. *Journal of Geophysical Research: Solid Earth*, 124(7):7231–7258, 2019.

S. Uyeda and H. Kanamori. Back-arc opening and the mode of subduction. *Journal of Geophysical Research: Solid Earth*, 84(B3):1049–1061, 1979.

M. Yamamoto, J. P. Morgan, and W. J. Morgan. Global plume-fed asthenosphere flow-i: motivation and model development. *SPECIAL PAPERS-GEOLOGICAL SOCIETY OF AMERICA*, 430:165, 2007.

Supporting Information for "The influence of a sub-lithospheric layer width on the partitioning of the induced mantle flow, surface motions and subduction dynamics"

R. Carluccio[a], L. N. Moresi[b], F. A. Capitanio [c], R. Farrington[a], L. Colli[d], B. R. Mather[8]

[a]School of Geography, Earth and Atmospheric Sciences, University of Melbourne, VIC, AU
[b]Research School of Earth Sciences, Australian National University, Canberra, ACT, AU
[c]School of Earth, Atmosphere and Environment, Monash University, Clayton, VIC, AU. Melbourne, VIC, AU
[d] Department of Earth and Atmospheric Sciences, University of Houston, Houston, TX, US
[e]EarthByte Group, School of Geoscience, The University of Sydney, Sydney, NSW, AU.

Contents of this file

1. Table S1
2. Figures from S1 to S2

Model parameters varied per set of simulation in this study						
# Set	**Model ID**	W_{OP}/W_{box}	W_{SLL}/W_{OP}	$\eta_M/\eta_{\mathrm{SLL}}$	L_{box} [km]	η_{LM}/η_{UM}
	RM	1	0	10^0	4000	-
1	M1-M4	1	1/4, 1/2, 3/4,1	10^2	4000	-
	M5-M9	1	1/4, 1/2, 3/4,1	10^1	4000	-
	M10	1/2	0	10^0	4000	-
2	M11-M14	1/2	1/4, 1/2, 3/4,1	10^2	4000	-
	M15-M19	1/2	1/4, 1/2, 3/4,1	10^1	4000	-
	M20	1	0	10^2	6000	30
3	M21	1	0	10^0	6000	30

Table 1: Parameters used and varied for the experiments performed during this study.

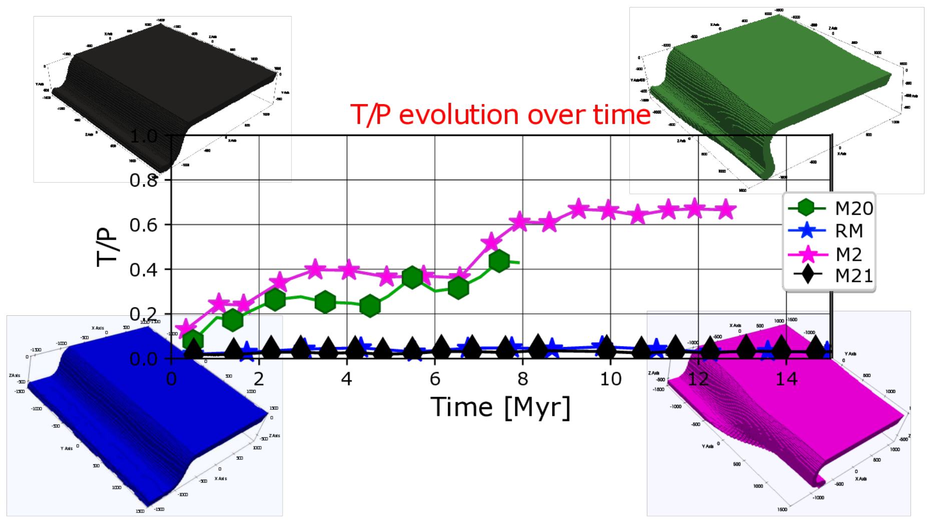

Figure 1: The comparison of the time evolution of the toroidal: poloidal amplitude ratio (T/P) of subduction models with a lower mantle, M20 ($\eta_{\mathrm{M}}/\eta_{\mathrm{SLL}}$=$10^2$) and M21 ($\eta_{\mathrm{M}}/\eta_{\mathrm{SLL}}$= 10^0) is shown in a comparison between the RM ($\eta_{\mathrm{M}}/\eta_{\mathrm{SLL}}$= 10^0) and M2 ($\eta_{\mathrm{M}}/\eta_{\mathrm{SLL}}$= 10^2). M20 and M21 cases have the same characteristics as M2 and RM, respectively, but they include a lower mantle that extends 800km depth, and an upper-lower mantle transition zone characterised by a viscosity contrast of 30. The figure also shows a comparison of the morphology assumed by he subducting slab at the steady state stage of the subduction evolution for the four models. The figure shows that similar trends are maintained in the evolution of T/P and slab subduction style with the inclusion of the lower mantle.

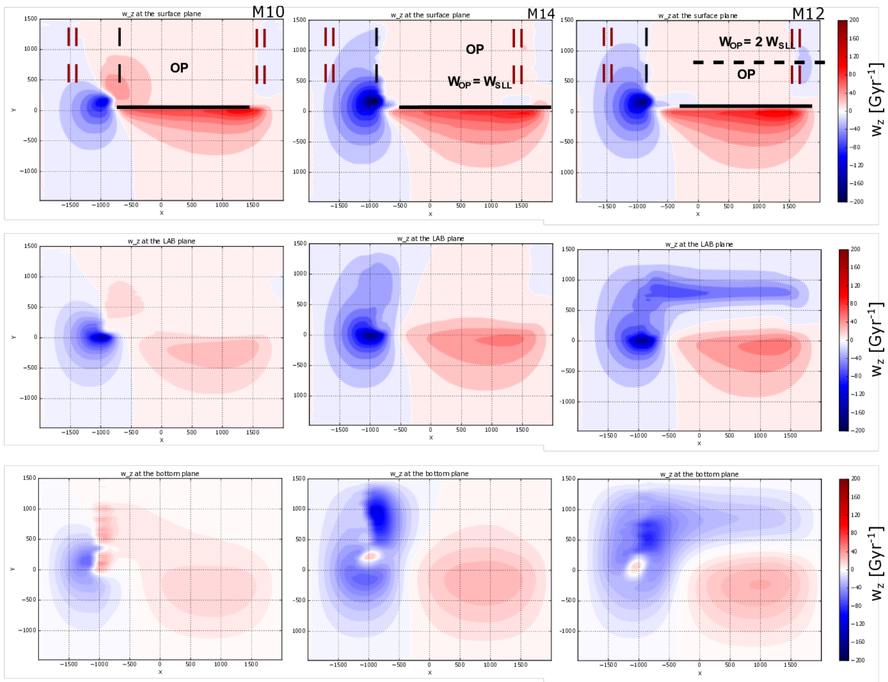

Figure 2: Radial vorticity field (left to right) of slab free-edge models where the plate width is half of the modelling box width. The comparison is shown among the M10 ($\eta_{\mathrm{M}}/\eta_{\mathrm{SLL}}$= 10^0 and $W_{SLL} = 0$), M14 ($\eta_{\mathrm{M}}/\eta_{\mathrm{SLL}}$= 10^2 with $W_{SLL} = W_{OP}$) and M12 ($\eta_{\mathrm{M}}/\eta_{\mathrm{SLL}}$=$10^2$ with $W_{SLL} = 1/2W_{OP}$) cases. The comparison is shown in the proximity of (top to bottom) the surface, lithosphere-asthenosphere boundary and 660 km bottom boundary of the model. All these models show an additional toroidal cell at the surface, which was not present in models with a continuous slab (figure 5 in the main manuscript). In M14 the strength of the toroidal cell is enhanced at depth by the presence of the SLL. In M12, there is an additional toroidal cell that develops beneath the base of a plate due to the presence of a non-uniform SLL.

Supporting Information for "The influence of a sub-lithospheric layer width on the partitioning of the induced mantle flow, surface motions and subduction dynamics"

R. Carluccio[a], L. N. Moresi[b], F. A. Capitanio [c], R. Farrington[a], L. Colli[d], B. R. Mather[8]

[a]School of Geography, Earth and Atmospheric Sciences, University of Melbourne, VIC, AU
[b]Research School of Earth Sciences, Australian National University, Canberra, ACT, AU
[c]School of Earth, Atmosphere and Environment, Monash University, Clayton, VIC, AU. Melbourne, VIC, AU
[d] Department of Earth and Atmospheric Sciences, University of Houston, Houston, TX, US
[e]EarthByte Group, School of Geoscience, The University of Sydney, Sydney, NSW, AU.

Contents of this file

Model parameters varied per set of simulation in this study						
# Set	**Model ID**	W_{OP}/W_{box}	W_{SLL}/W_{OP}	$\eta_M/\eta_{\mathrm{SLL}}$	L_{box} [km]	η_{LM}/η_{UM}
	RM	1	0	10^0	4000	-
1	M1-M4	1	1/4, 1/2, 3/4,1	10^2	4000	-
	M5-M9	1	1/4, 1/2, 3/4,1	10^1	4000	-
	M10	1/2	0	10^0	4000	-
2	M11-M14	1/2	1/4, 1/2, 3/4,1	10^2	4000	-
	M15-M19	1/2	1/4, 1/2, 3/4,1	10^1	4000	-
	M20	1	0	10^2	6000	30
3	M21	1	0	10^0	6000	30

Table 1: Parameters used and varied for the experiments performed during this study.

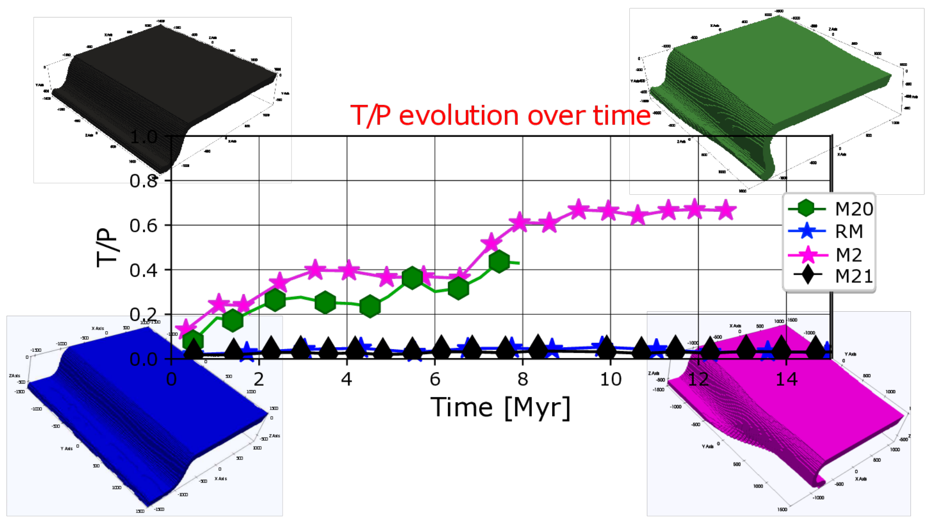

Figure 1: The comparison of the time evolution of the toroidal: poloidal amplitude ratio (T/P) of subduction models with a lower mantle, M20 ($\eta_{\mathrm{M}}/\eta_{\mathrm{SLL}}$=$10^2$) and M21 ($\eta_{\mathrm{M}}/\eta_{\mathrm{SLL}}$= 10^0) is shown in a comparison between the RM ($\eta_{\mathrm{M}}/\eta_{\mathrm{SLL}}$= 10^0) and M2 ($\eta_{\mathrm{M}}/\eta_{\mathrm{SLL}}$= 10^2). M20 and M21 cases have the same characteristics as M2 and RM, respectively, but they include a lower mantle that extends 800km depth, and an upper-lower mantle transition zone characterised by a viscosity contrast of 30. The figure also shows a comparison of the morphology assumed by he subducting slab at the steady state stage of the subduction evolution for the four models. The figure shows that similar trends are maintained in the evolution of T/P and slab subduction style with the inclusion of the lower mantle.

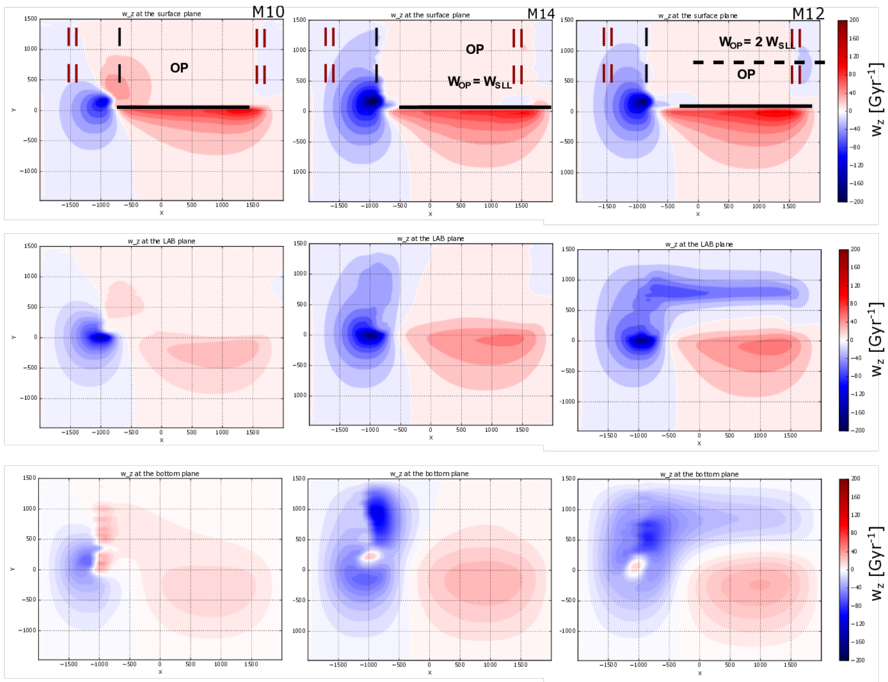

Figure 2: Radial vorticity field (left to right) of slab free-edge models where the plate width is half of the modelling box width. The comparison is shown among the M10 ($\eta_{\mathrm{M}}/\eta_{\mathrm{SLL}}= 10^0$ and $W_{SLL} = 0$), M14 ($\eta_{\mathrm{M}}/\eta_{\mathrm{SLL}}= 10^2$ with $W_{SLL} = W_{OP}$) and M12 ($\eta_{\mathrm{M}}/\eta_{\mathrm{SLL}}=10^2$ with $W_{SLL} = 1/2W_{OP}$) cases. The comparison is shown in the proximity of (top to bottom) the surface, lithosphere-asthenosphere boundary and 660 km bottom boundary of the model. All these models show an additional toroidal cell at the surface, which was not present in models with a continuous slab (figure 5 in the main manuscript). In M14 the strength of the toroidal cell is enhanced at depth by the presence of the SLL. In M12, there is an additional toroidal cell that develops beneath the base of a plate due to the presence of a non-uniform SLL.